

# Micro-strain Evolution and Toughening Mechanisms in a Trimodal Al-Based Metal Matrix Composite

YUZHENG ZHANG, TROY D. TOPPING, HANRY YANG, ENRIQUE J. LAVERNIA, JULIE M. SCHOENUNG, and STEVEN R. NUTT

A trimodal metal matrix composite (MMC) based on AA (Al alloy) 5083 (Al-4.4Mg-0.7Mn-0.15Cr wt pct) was synthesized by cryomilling powders followed by compaction of blended powders and ceramic particles using two successive dual mode dynamic forgings. The microstructure consisted of 66.5 vol pct ultrafine grain (UFG) region, 30 vol pct coarse grain (CG) region and 3.5 vol pct reinforcing boron carbide particles. The microstructure imparted high-tensile yield strength (581 MPa) compared to a conventional AA 5083 (242 MPa) and enhanced ductility compared to 100 pct UFG Al MMC. The deformation behavior of the heterogeneous structure and the effects of CG regions on crack propagation were investigated using *in situ* scanning electron microscopy micro-tensile tests. The micro-strain evolution measured using digital image correlation showed early plastic strain localization in CG regions. Micro-voids due to the strain mismatch at CG/UFG interfaces were responsible for crack initiation. CG region toughening was realized by plasticity-induced crack closure and zone shielding of disconnected micro-cracks. However, these toughening mechanisms did not effectively suppress its brittle behavior. Further optimization of the CG distribution (spacing and morphology) is required to achieve toughness levels required for structural applications.

DOI: 10.1007/s11661-014-2729-8

© The Minerals, Metals & Materials Society and ASM International 2014

## I. INTRODUCTION

OVER the past few decades, nanocrystalline (NC) and ultrafine-grained (UFG) materials have drawn attention due to the improved mechanical properties and the unusual grain structures.<sup>[1–5]</sup> A wide variety of synthesis techniques have been reported to fabricate bulk NC or UFG materials.<sup>[6,7]</sup> Among them, cryomilling is a promising synthesis method for making NC or UFG materials in commercial quantities (30 to 40 kg).<sup>[8–10]</sup> During cryomilling, gas-atomized metallic powders undergo severe plastic deformation *via* high-energy ball milling in cryogenic liquid slurry. During cryomilling these powders are sheared, fractured, and cold-welded back together refining the grain size to the NC regime. The grain refinement process during milling can be divided into three major stages<sup>[11]</sup>: (1) localization of high dislocation densities into shear bands, (2) low-angle grain boundaries (LAGBs) and subgrains evolving from dislocation rearrangement at particular strain levels *via*

recovery, and (3) LAGBs transforming to high-angle grain boundaries (HAGBs) with excessive deformation by GB sliding and rotation. Cryogenic temperature effectively dissipates the heat generated from milling and thus limits recovery and grain growth.<sup>[9]</sup> In this study, Al alloy (AA) 5083 was selected as base material because of its potential application in automobile, aerospace and marine structures. Cryomilled Al alloy exhibits enhanced thermal stability due to the creation of nanodispersed aluminum nitrides that pin grain boundaries and allow for the NC or UFG microstructure to be preserved during thermomechanical processing and consolidation.<sup>[9,12–16]</sup> Since cryomilled AA 5083 retain its refined grain structures, the strength of the resultant bulk products are significantly enhanced according to the Hall–Petch strengthening mechanism.<sup>[9,17,18]</sup> However, NC or UFG materials usually suffer from limited ductility and low toughness owing to minimal work hardening associated with NC or UFG regions.<sup>[19,20]</sup> This limitation precludes the use of NC and UFG materials from most engineering applications.

In an effort to enhance plasticity and mitigate the brittle behavior of cryomilled AA 5083 (Al-4.4Mg-0.7Mn-0.15Cr wt pct) coarse grain (CG) regions were introduced into a UFG matrix.<sup>[8,21]</sup> One appeal of cryomilling is the ability to design multi-scale grain structure by simply blending unmilled powders with milled powders.<sup>[22–24]</sup> Similarly, one can produce a metal matrix composite (MMC) by adding reinforcing ceramic particles during milling.<sup>[25]</sup> In this work, a trimodal microstructure was achieved by introducing coarse grain (CG) regions into a UFG matrix reinforced by boron carbide (B<sub>4</sub>C) particles. The introduction of CG regions

YUZHENG ZHANG, Research Assistant, and STEVEN R. NUTT, Professor, are with the Department of Chemical Engineering and Materials Science, University of Southern California, Los Angeles, CA 90089. Contact e-mail: yuzhengz@usc.edu TROY D. TOPPING, Assistant Professor, is with the Department of Chemical Engineering and Materials Science, University of California, Davis, Davis, CA 95616, and also with the Department of Mechanical Engineering, California State University, Sacramento, Sacramento, CA 95819. HANRY YANG, Research Assistant, ENRIQUE J. LAVERNIA and JULIE M. SCHOENUNG, Professors, are with the Department of Chemical Engineering and Materials Science, University of California, Davis.

Manuscript submitted August 27, 2014.

Article published online January 7, 2015

reportedly improves the ductility of cryomilled Al with only a moderate strength penalty,<sup>[24,25]</sup> and B<sub>4</sub>C was selected because it is the third hardest material known to man, surpassed only by diamond and cubic boron nitride. Strong covalent bonds in B<sub>4</sub>C impart an extraordinarily high hardness (25 to 40 GPa) but low density (~2.5 g cm<sup>-3</sup>).<sup>[26]</sup>

Understanding the deformation and failure mechanisms associated with this heterogeneous microstructure is essential to evaluate this complex microstructural design and further improvement of the mechanical properties. Lee<sup>[23]</sup> proposed a toughening mechanism for a bimodal UFG Al-Mg alloy and schematically illustrated the crack propagation through CG and UFG regions. Zhang<sup>[27]</sup> discussed the fracture mechanism of a UFG Al composite based on fracture analysis showing shear band formation in UFG region followed by void initiation and micro-crack propagation. Fan<sup>[22]</sup> reported a combined fracture mode of shear localization, cavitation, and necking for a bimodal UFG Al-Mg alloy under compressive tests. However, these post-failure analyses did not provide clear answers to several key questions, such as (1) how micro-strain evolves in this multi-scale grain structure, (2) how cracks interact with CG regions along the propagation path, and (3) what toughening mechanism(s) arise from the ductile CG constituent. An *in situ* observation technique is one approach to answering these questions. To our knowledge, no *in situ* straining experiments have been conducted to directly observe the deformation and fracture behavior of a cryomilled trimodal Al MMC. In this work, we analyzed micro-strain evolution, crack propagation, and CG toughening mechanisms at the micron scale using *in situ* tensile straining in a scanning electron microscopy (SEM). Digital image correlation (DIC) was used to quantify the micro-strain development within the heterogeneous microstructure of the trimodal MMC during a tensile test. According to the findings from the *in situ* tensile test, the toughening effectiveness of the CG inclusions was limited by sub-optimal CG distribution, resulting in a tensile failure strain of 3.9 pct.

## II. EXPERIMENTAL PROCEDURE

### A. Material Synthesis

Nanocrystalline AA 5083—B<sub>4</sub>C MMC powders were synthesized using a modified 1S Svevari attritor by ball milling in a liquid nitrogen slurry at cryogenic temperature (cryomilling). Gas-atomized AA 5083 powders obtained from Valimet, Inc. (Stockton, CA) were blended with submicron B<sub>4</sub>C particulates obtained from H.C. Starck (Newton, MA) with an average size of ~500 nm. This powder blend was then cryomilled for 12 hours at 180 rpm with a 32:1 ball-to-powder ratio and 0.2 wt pct stearic acid (CH<sub>3</sub>(CH<sub>2</sub>)<sub>16</sub>CO<sub>2</sub>H). Stearic acid was used as process control agent (PCA) to prevent excessive cold welding during cryomilling. Unmilled (as atomized) AA 5083 powder was blended with cryomilled powder to reach a target composition of 66.5 vol pct UFG Al, 30 vol pct CG Al, and 3.5 vol pct B<sub>4</sub>C

reinforcing particles. To remove any residual moisture or PCA, the powder blend was containerized in an Al 6061 can and hot vacuum degassing at 773 K (500 °C) for 20 hours with a final vacuum level less than  $1.0 \times 10^{-6}$  torr.<sup>[28]</sup> The degassed powders were consolidated at Advanced Materials and Manufacturing Technologies (Riverbank, CA) using dual mode dynamic (DMD) forging—a quasi-isostatic forging process. During DMD forging, uniaxial compression was converted to a quasi-isostatic pressure *via* a granular pressure transmitting medium (PTM), surrounding the target material. DMD forging was performed at 673 K (400 °C) twice to consolidate the powders and deform the bulk sample (after the containment can was removed) to its final shape.

### B. Characterization

The microstructures of this trimodal AA 5083 MMC and a conventional, armor grade AA 5083 H131 sample were characterized using a field-emission SEM (JSM-7001F, JEOL Inc.). The conventional material, used as a baseline for comparison, is a strain-hardened plate of AA 5083 produced *via* ingot metallurgy, where the H 131 is a temper designation that refers to the degree of strain hardening in the cold-rolled plate.<sup>[29]</sup> The grain structures of the conventional AA 5083 and CG regions of the trimodal sample were analyzed using electron backscattered diffraction (EBSD). Due to the difficulty of indexing UFG regions of trimodal nano-composite using conventional EBSD, the grain structure of UFG regions was determined using transmitted Kikuchi diffraction (TKD).<sup>[30,31]</sup> The experimental setup for TKD collection is illustrated in Figure 1(a). A thin foil specimen was mounted on a TEM specimen blade and tilted from horizontal orientation by 20 deg as shown in Figure 1(a). The Kikuchi pattern was collected using an accelerating voltage of 20 kV at a working distance of 12 mm. The thin specimen used in the TKD technique was prepared using a focused ion beam (FIB: JIB-4500, JEOL Inc.) and mounted on a copper grid as shown in Figure 1(b).

### C. Mechanical Testing

Tensile tests were performed *in situ* in a SEM (JSM-6610, JEOL Inc.) using the micro-tensile stage as shown in Figure 2(a). The samples were electrical discharge machined (EDM'd) to a miniature dog-bone specimen as shown schematically in Figure 2(b). In order to predict where failure will occur, a notch was deliberately made at the gage center to introduce a stress concentration on the target area. The tensile test was conducted using a strain rate of  $4.18 \times 10^{-4}$  s<sup>-1</sup> at room temperature. The tensile test was paused every 10 seconds to record SEM images of regions of interest. Each SEM image was centered on the same surface feature to ensure every image was captured at the identical location. These SEM images of deforming regions were subsequently exported to DIC software for micro-strain calculation. Details in DIC settings can be found elsewhere.<sup>[32]</sup> Hardness of H131 and trimodal samples

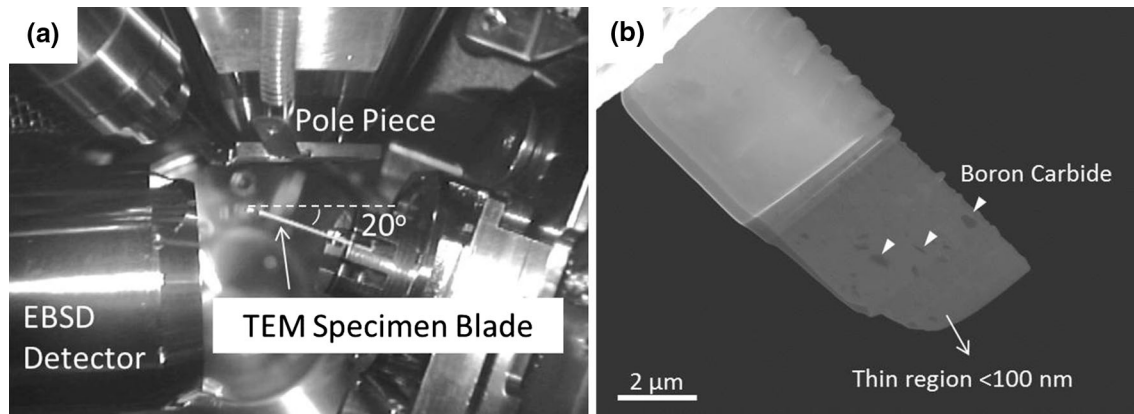


Fig. 1—(a) SEM chamber setup for TKD, (b) thin film sample for TKD prepared using FIB.

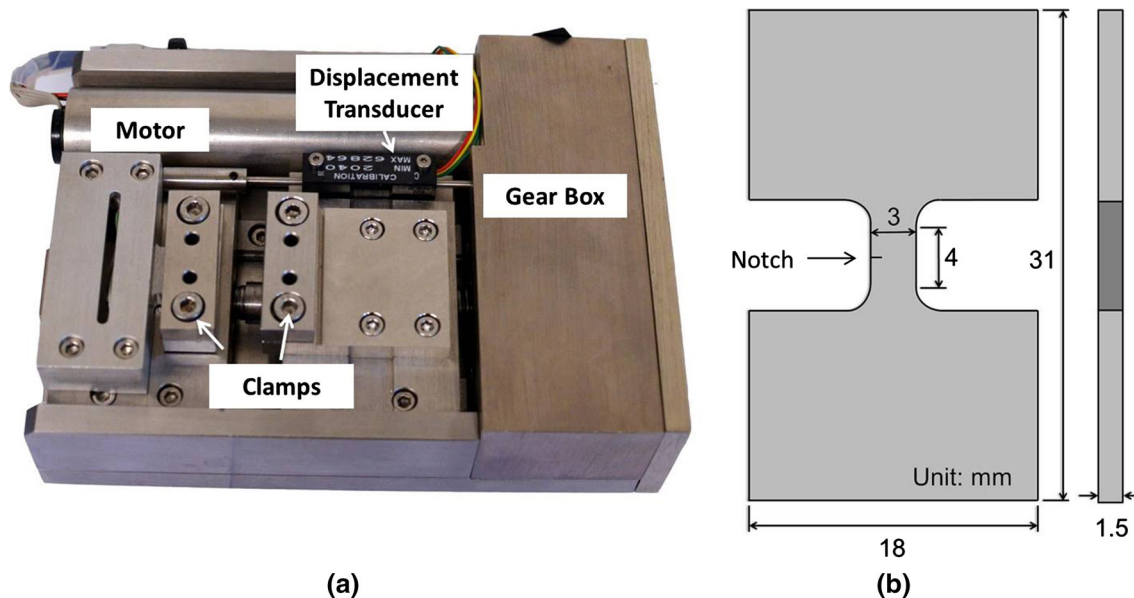


Fig. 2—(a) Picture of the micro-tensile stage, (b) dimensions of a miniature dog-bone tensile specimen.

was measured using instrumented indentation testing (NanoXP, MTS). Failure analysis was conducted on the fractured surface after tensile tests.

### III. RESULTS AND DISCUSSION

#### A. Microstructure

The microstructure of the trimodal Al-based MMC was imaged using backscattered electron signals in SEM. The bright CG regions were uniformly distributed in a dark UFG matrix, as shown in Figure 3(a). The CG regions had an average size of  $165.7 \mu\text{m}$  and comprised 28.1 pct of the cross-sectional area, which is consistent with the volume fraction of unmilled powders blended during synthesis. The average spacing between adjacent CG regions is  $\sim 150 \mu\text{m}$ . The CG powders showed an aspect ratio of  $\sim 2.3$  due to flattening during consolidation. The dark tone in the UFG matrix was caused by  $\text{B}_4\text{C}$  particulates introduced during cryomilling. As

shown in Figure 3(b), no  $\text{B}_4\text{C}$  was observed in CG regions (CG powders were added after cryomilling). In Figure 3(c),  $\text{B}_4\text{C}$  particles showed faceted shapes with an average size of 315 nm and an approximately uniform dispersion in UFG matrix.

In addition to the dark  $\text{B}_4\text{C}$  particles, bright particles of similar size were present in both UFG and CG regions (see red arrow in Figure 3(c)). A portion of these bright particles were clustered at UFG–CG interface regions. Energy-dispersive X-ray spectroscopy (EDX) revealed that these particles presented Mn and Fe K lines (Figure 3(d)). Thus, these bright particles were identified as second-phase intermetallic particles (SPIPs), such as  $\text{Al}_6(\text{Mn,Fe})$ .<sup>[33]</sup> These are normally present as grain refining dispersoids in AA 5083, and were refined during cryomilling and thermomechanical processing (TMP).<sup>[34,35]</sup> These closely spaced, submicron-sized particles potentially can provide Orowan strengthening in both CG and UFG regions.<sup>[25,36]</sup> However, these SPIPs may also reduce fracture tough-



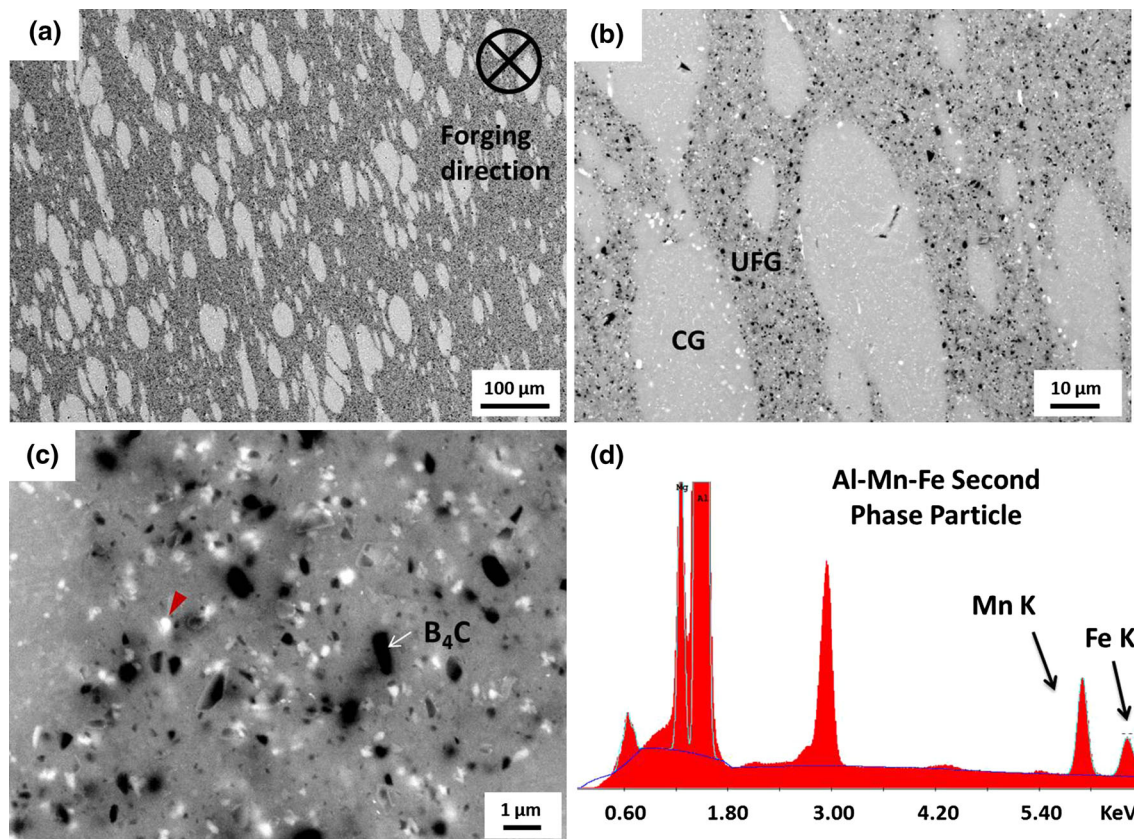


Fig. 3—Backscattered SEM images of the microstructure of the trimodal sample at (a) low, (b) medium, and (c) high magnifications. (d) Energy-dispersive X-ray spectrum of  $\text{Al}_6(\text{Mn,Fe})$  second-phase intermetallic particles (SPIPs).

ness, as they are generally brittle and may provide sites for early crack nucleation. Their influence on fracture toughness requires future investigation. Close examination of SEM images showed no voids or defects in either CG or UFG regions or at the  $\text{Al}/\text{B}_4\text{C}$  interface before tensile loading. This observation indicated that DMD forging was effective in consolidating Al powders to full density and eliminating pre-existing micro-voids or micro-cracks.

Crystalline orientation maps of the trimodal and H131 samples were acquired to measure the average grain size using EBSD. To achieve a high index rate of UFG regions in the trimodal sample, TKD<sup>[30,31]</sup> was used to collect Kikuchi patterns as shown in Figure 4(a). The spatial resolution using TKD (<10 nm) was significantly better than conventional EBSD because the electron probe did not produce a broad interaction volume in the thin TEM specimens. Each orientation map was cleaned using confidence index (CI) standardization followed by single iteration grain dilation. Pixels with low CI (<0.1) caused by  $\text{B}_4\text{C}$  or SPIPs were excluded from the map as indicated by black areas in Figure 4(a). The average grain sizes in UFG, CG regions, and H131 were 197 nm, 1.3, and 25.9  $\mu\text{m}$ , respectively. The grain shape aspect ratio in UFG, CG regions, and H131 were 0.42, 0.54, and 0.44, respectively. The CG regions in the trimodal sample exhibited certain textures. For example, the CG region in Figure 4(b) showed (101) texture. CG regions are likely to

have textures because most CG powders were single-crystalline particles before consolidation. During consolidation process, subgrain boundaries were introduced in CG regions which inherit textures from their original crystalline orientations. On the other hand, the UFG region in the trimodal sample and the conventional H131 sample did not have preferred crystalline orientations (see Figures 4(a) and (b)) because grain refinement during cryomilling leads to high-angle grain boundaries and random crystalline orientations.

To evaluate hardness, at least 30 indents were measured for each region using an instrumented nano-indenter with a Berkovich tip. Hardness was plotted against  $(\text{grain size})^{-1/2}$  (see Figure 5) indicating that the grain size strengthening effect followed the Hall–Petch relationship<sup>[37,38]</sup> in a range from  $\sim 30 \mu\text{m}$  down to  $\sim 200 \text{ nm}$  in grain size. However, determination of the Hall–Petch coefficient was not possible due to the large variation in hardness values. This variation is especially evident for the UFG matrix in the trimodal sample because the true hardness value of AA 5083 grains in UFG regions was inevitably biased by the presence of nearby  $\text{B}_4\text{C}$  and  $\text{Al}_6(\text{Mn,Fe})$  dispersoids. The hardness variation for the CG regions is attributed to different textures and  $\text{Al}_6(\text{Mn,Fe})$  dispersoids in the CG regions. The Hall–Petch coefficient of AA 5083 was well documented in the literature.<sup>[9]</sup> Table I presents a summary of the morphology, average grain size, and hardness of each region in trimodal and H131 samples.

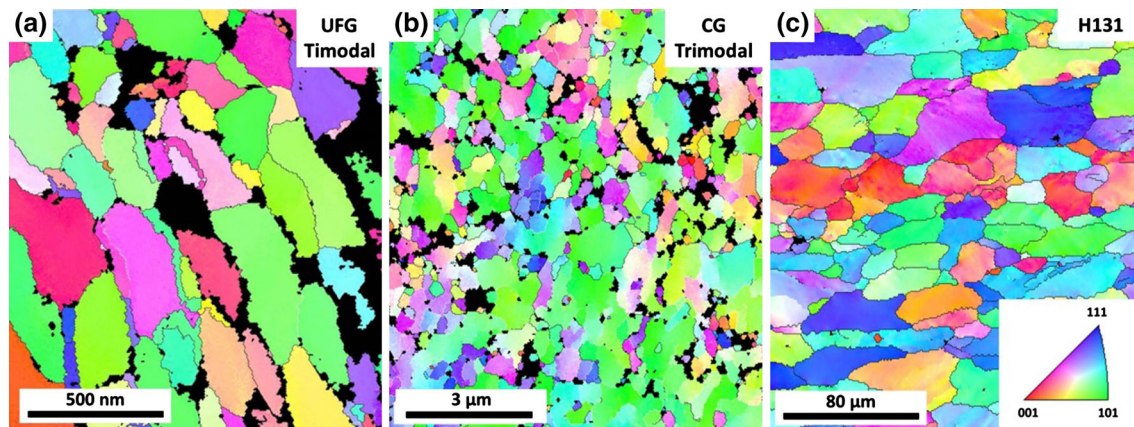


Fig. 4—(a) Crystalline orientation map of UFG regions in the trimodal sample collected by TKD. (b) Crystalline orientation map of CG regions in the trimodal sample and (c) H131 using conventional EBSD.

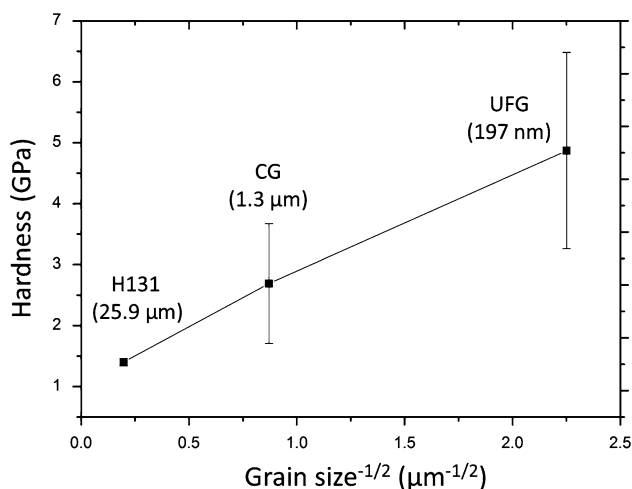


Fig. 5—Plot of hardness vs grain size<sup>-1/2</sup> indicating that Hall-Petch relationship applies in a range from ~30 μm down to ~200 nm in grain size.

### B. In Situ Tensile Testing

Engineering stress-strain curves from the micro-tensile tests are plotted in Figure 6. The serrated yielding (Figure 6) in the H131 curve was due to dynamic strain aging (DSA) or Portevin-Le Chatelier effect, which is common in ductile solid-solution materials.<sup>[39]</sup> DSA was not observed in the trimodal curve, indicating low dislocation mobility and limited work hardening.<sup>[40,41]</sup>

The 0.2 pct offset yield strength, ultimate tensile stress (UTS), and elongation to failure  $\epsilon_f$  for trimodal and H131 samples are tabulated in Table II. The yield strength of the trimodal Al-based MMC (581 MPa) was twice that of the conventional H131 sample (242 MPa). The enhanced strength is attributed primarily to the refined grain structure and presence of reinforcing  $B_4C$  particles. A more complete analysis of the strengthening mechanisms present in trimodal composites can be found in Reference 42. The trimodal sample showed 3.9 pct elongation to failure  $\epsilon_f$  with no necking in the gage area prior to failure. When compared to H131, the

Table I. Summary of the Microstructure and Hardness Values for CG Region, UFG Region, and  $B_4C$  of the Trimodal Sample and for the H131 Sample

	Avg. Grain Size	Avg. Grain Aspect Ratio	Avg. Region/Particle Size	Hardness (GPa)
CG	1.3 μm	0.54	165.7 μm	2.69 ± 0.98
UFG	197 nm	0.42	—	4.87 ± 1.61
H131	25.9 μm	0.44	—	1.40 ± 0.06
$B_4C$	—	—	315 nm	24.8 ± 5.56

trimodal sample appears to fracture at a relatively low strain with little evidence of work hardening. However, many carbide reinforced MMCs, such as Al-SiC MMCs<sup>[43]</sup> are naturally brittle in tension, and therefore, the observed tensile ductility of the trimodal sample (with both carbide reinforcement and UFG regions) is significant. Therefore, the remarkable tensile ductility in the Al- $B_4C$  MMC is attributed to the CG content in the trimodal microstructure.

The strain-to-failure values presented in this work are higher than those reported in standard tests due to the size effect, instrument compliance, and low strain rate. The tensile specimens used in this work have reduced sizes and customized geometry to fit in the micro-tensile module. Therefore, larger strain-to-failure values can be partially caused by the size effect.<sup>[44]</sup> Instrument compliance is not negligible when testing high-strength trimodal specimens. The deformation of the micro-tensile module contributed to the derived strain as well.<sup>[44]</sup> The low strain rate ( $\sim 10^{-4} \text{ s}^{-1}$ ) used in this work is another reason for higher strain-to-failure values. All the tensile tests in this work were conducted using the same sample geometry and the same testing condition to allow direct comparison between non-standard tests.

### C. Micro-strain Measurement

The evolution of micro-strain in the trimodal Al-based MMC was analyzed using DIC, a technique that can be used to calculate and visualize the micro-strain field on a deforming surface during micro-tensile testing.



For DIC, an isotropic random speckle pattern is required on the specimen surface to track the full-field surface deformation. After vibratory polishing, the dispersed  $B_4C$  particles and SPIPs serendipitously provided intrinsic speckle patterns for a field of view of  $\sim 50$  by  $50\ \mu\text{m}$ .

Using DIC, the micro-strain field near the notch area at the yielding stage was mapped, as shown in Figure 7. During the early stage of deformation, elastic displacements occurred evenly in UFG and CG regions. As tensile loading increased, CG regions began to yield, owing to the lower yield strength compared to the UFG matrix, while UFG regions continued to deform elastically. As a result, the evolving plastic strain was

localized primarily in CG regions, as shown in Figure 7(b). Similar finding was observed in UFG Al alloys with a bimodal grain structure.<sup>[45]</sup>

However, as strain increased, voids and cracks formed between the CG regions and the UFG matrix. Figure 8 shows micro-cracks at CG/UFG interfaces prior to fracture. Voids and cracks were absent prior to loading, so these micro-cracks formed during deformation due to stress concentrations, and subsequently evolved to form macro-cracks. From Figure 8, note that a shear band is present in the CG region but not in the UFG matrix. The observation supports the hypothesis that CG regions bear more plastic strain than the UFG matrix during deformation. As indicated by arrows in Figure 8, micro-cracks also formed at large inclusions of SPIP.

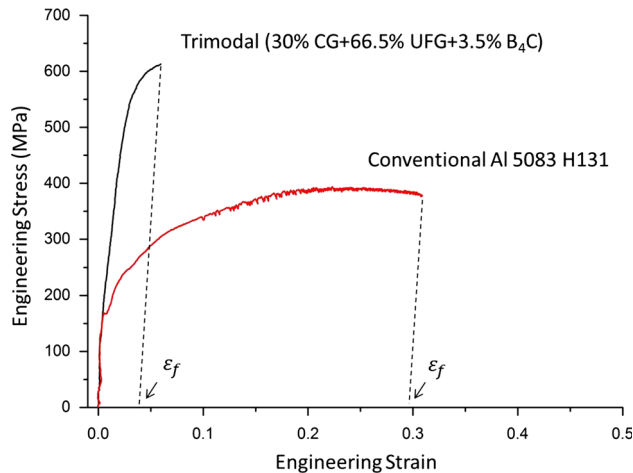


Fig. 6—Engineering stress and strain curves for the trimodal and H131 samples.

**Table II. Mechanical Properties of the Trimodal Al-Based MMC and H131 Sample**

	Yield Strength (MPa)	UTS (MPa)	Elongation to Failure, $\epsilon_f$ (pct)
Trimodal	581	613	3.9
H131	242	394	29.6

#### D. Toughening Mechanisms

Toughening mechanisms were revealed through dynamic observations of crack growth during *in situ* straining experiments. These experiments were undertaken to understand how cracks interacted with the CG regions, which were intended to enhance ductility and toughness at a moderate cost in strength.<sup>[46,47]</sup> Two toughening mechanisms were identified from the *in situ* straining experiments. First, cracks were blunted in the CG region due to plasticity. When a crack reached a CG region, it was arrested, blunted, and deflected, as shown in Figure 9(a). Shear banding extended across this CG region. Second, cracks were arrested in CG regions through zone shielding of disconnected micro-cracks and micro-voids along the path of the shear band, as indicated in Figure 9(b) (arrows). These micro-cracks and micro-voids effectively relaxed the stress triaxiality at the crack tip. As a result, the propagating crack tip deflected and advanced through the relatively brittle UFG matrix. Complete decohesion was not observed at the CG/UFG interface, indicating a strong metallurgical bond between the CG and UFG regions.

The observations described above revealed the role of CG regions in toughening the trimodal composite. However, these toughening mechanisms were limited by the availability of pathways for brittle crack propagation in the UFG matrix. As cracks lengthened, the

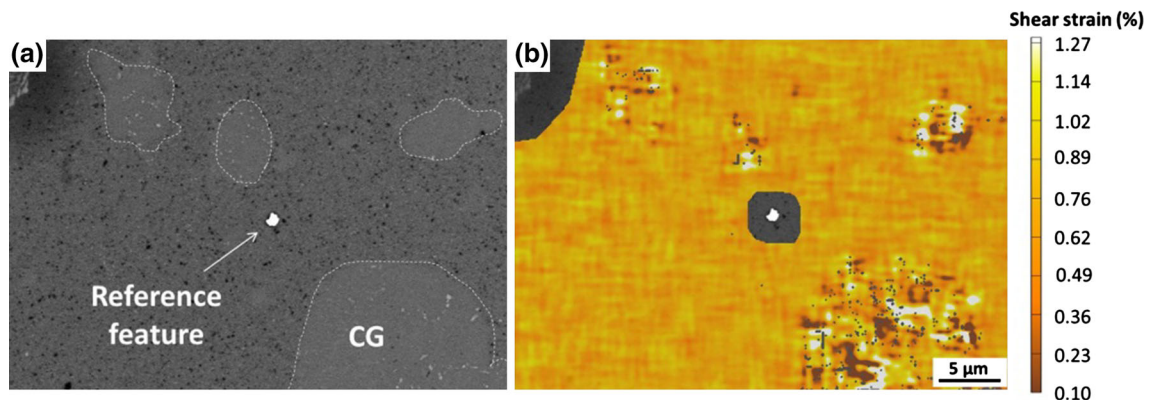


Fig. 7—(a) SEM micrograph of the region of interest in DIC micro-strain analysis, CG regions highlighted with dash line boundaries, (b) DIC strain field map of the same area showing development of localized micro-strain in CG regions.

stress intensity factor increased at the crack tip, and the ductile CG regions were eventually unable to restrain the crack. Consequently, despite localized ductility, the trimodal sample fractured in a brittle manner. The ductile behavior stemmed from deformation of CG regions before the crack propagation prevailed in the UFG matrix.

Ductile phase toughening depends strongly on the morphology and the distribution of the ductile phase in the brittle matrix. For example, a Zr-Ti-based bulk metallic glass (BMG) toughened with ductile crystalline dendrites led to extraordinary toughness and tensile ductility comparable to crystalline Ti alloys.<sup>[48]</sup> The success of this approach rested largely on achieving a particular distribution (spacing and size) of the ductile dendritic arms. A similar approach should be effective with the UFG–CG grain structure considered here. For example, a CG/UFG laminate structure or a UFG matrix with a CG network would effectively deflect and trap cracks at the early stage of crack formation. Such

microstructures can be achieved by multiple approaches. For example, one can alter the size (and amount) of the unmilled powders blended with the cryomilled powders to control spacing. Alternatively, one can employ an additional SPD step such as high pressure torsion (HPT) or equal channel angular pressing (ECAP) to alter the shape and spacing of the CG regions to laminate structures without significant grain refinement.

The microstructural length scale ( $L$ ) and spacing ( $S$ ) of CG inclusions can be optimized when  $L$  and  $S \approx r_p$ , where  $r_p$  is the characteristic size of the plastic zone associated with the crack tip.<sup>[48]</sup> Assuming a mode I opening crack and plane stress condition (surface cracks),  $r_p$  is given by the equation below.<sup>[49]</sup>

$$r_p = \frac{K_{IC}^2}{\pi \sigma_y^2},$$

where  $K_{IC}$  and  $\sigma_y$  are fracture toughness and yield strength, respectively. For plane strain condition (inter-

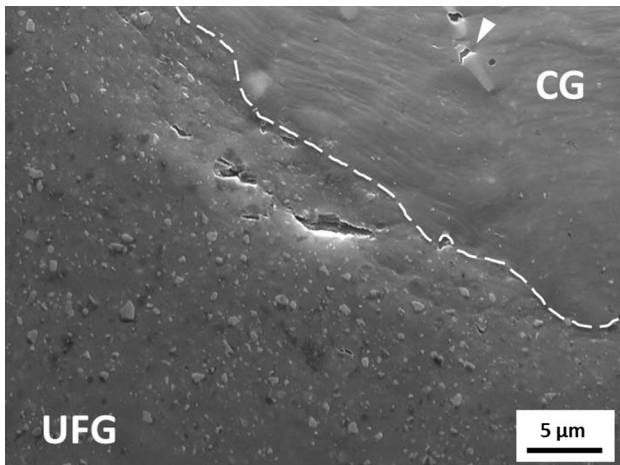


Fig. 8—SEM micrograph of micro-voids formation due to a strain mismatch between CG and UFG regions; Crack nucleation found in large inclusions of SPIIP, indicated by the arrow.

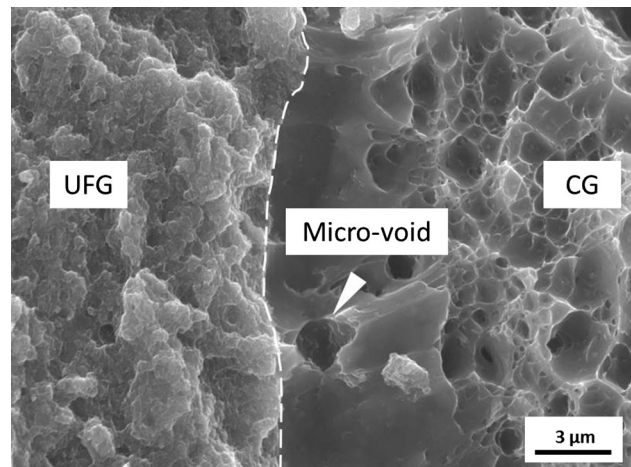


Fig. 10—SEM micrograph showing a fracture surface at the CG/UFG interface.

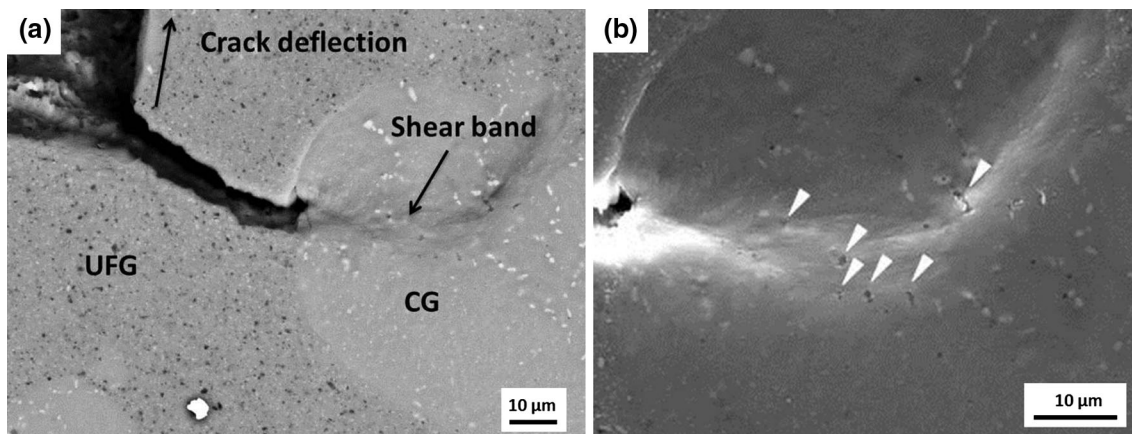


Fig. 9—(a) SEM backscattered electron micrograph showing a blunted crack tip trapped in a CG region and a deflected crack propagating in UFG region. (b) SEM secondary electron micrograph showing disconnected micro-cracks or micro-voids along the path of the shear band.

nal cracks), the plastic zone size will be  $\sim 1/6$  of the above value. We can choose the fracture toughness of a bimodal AA 5083 ( $\sim 10 \text{ MPa m}^{1/2}$ ) as a conservative estimate.<sup>[50]</sup> The yield strength on the other hand, can be taken from the *in situ* tensile tests reported here. Although the *in situ* test is not a standard test, this strength value can be used as a reasonable estimate, because sample geometry has negligible effect on yield strength.<sup>[44]</sup> The  $r_p$  for the UFG matrix can be estimated as  $r_p \approx 10$  to  $50 \mu\text{m}$ , indicating that the optimal toughening effect can be achieved when the size and spacing of CG inclusions are on the order of 10 to  $50 \mu\text{m}$ . For the current trimodal sample, the average size and spacing of CG inclusions are in the order of  $\sim 150 \mu\text{m}$  which are sub-optimal in terms of toughening effectiveness.

### E. Fracture Analysis

The fracture surface of the trimodal Al-based MMC was examined after micro-tensile testing. Figure 10 shows a portion of the fracture surface at a CG/UFG interface. The region illustrates the dual failure modes of brittle intergranular fracture in the UFG matrix and a dimpled ductile fracture in the CG region. The relatively smooth layer between the UFG and CG region arose from strain localization in CG regions prior to fracture. Micro-voids were present in this layer, but full-length decohesion between the CG and UFG regions was not observed. Negligible plastic flow was evident in the UFG matrix. Instead, the plastic flow in this trimodal Al-based MMC was largely confined to CG regions, which effectively blunted propagating cracks.

## IV. CONCLUSIONS

In this work, a trimodal MMC was synthesized by cryomilling, blending with unmilled powders, and hot consolidation *via* DMD forging. Micro-strain development and failure mechanisms were observed directly *via in situ* micro-tensile tests in a SEM. The *in situ* observations demonstrated that the ductile CG regions were only partly effective in blunting cracks that initiated in the UFG regions. Modifying the distribution (spacing and morphology) of the ductile CG regions holds promise as a means to more effectively toughen this brittle MMC. The cryomilling synthesis route—blending milled and unmilled powders, affords direct control of the distribution more readily than other processing methods. Furthermore, the morphology of the CG regions can be modified/optimized by secondary SPD processes (*e.g.*, HPT or ECAP) to arrest or delay crack growth more effectively at the early stage of deformation. Systematic effort to control the distribution and morphology of ductile CG inclusions promises to provide clearer understanding of crack growth mechanisms in bimodal alloys and provide guidelines for design of UFG microstructures with enhanced strength and toughness.

## ACKNOWLEDGMENTS

The authors gratefully acknowledge J. Curulli and M. Mecklenburg for their valuable advice. The images and data used in this article were generated at the Center for Electron Microscopy and Microanalysis (CEMMA), University of Southern California. The authors wish to acknowledge the financial support provided by the Office of Naval Research under the guidance of Rod Peterson and Bill Golumbskie (ONR Contract N00014-12-C-0241).

## REFERENCES

1. H. Gleiter: *Progress Mater. Sci.*, 1990, vol. 33, pp. 223–315.
2. R. Birringer: *Mater. Sci. Eng. A*, 1989, vol. 117, pp. 33–43.
3. C. Suryanarayana: *Int. Mater. Rev.*, 1995, vol. 40 (2), pp. 41–64.
4. K. Lu: *Mater. Sci. Eng. R*, 1996, vol. 16, pp. 161–221.
5. H. Gleiter: *Acta Mater.*, 2000, vol. 48, pp. 1–29.
6. M.A. Meyers, A. Mishra, and D.J. Benson: *Prog. Mater. Sci.*, 2006, vol. 51 (4), pp. 427–556.
7. R. Valiev, R. Islamgaliev, and I. Alexandrov: *Prog. Mater. Sci.*, 2000, vol. 45 (2), pp. 103–89.
8. V.L. Tellkamp, A. Melmed, and E.J. Lavernia: *Metall. Mater. Trans. A*, 2001, vol. 32A, pp. 2335–43.
9. D.B. Witkin and E.J. Lavernia: *Prog. Mater. Sci.*, 2006, vol. 51 (1), pp. 1–60.
10. A.P. Newbery, B. Ahn, T.D. Topping, P.S. Pao, S.R. Nutt, and E.J. Lavernia: *J. Mater. Proc. Technol.*, 2008, vol. 203 (1–3), pp. 37–45.
11. G. Hardenbergstr: *Nanostructured Mater.*, 1995, vol. 6 (95), pp. 33–42.
12. R.W. Hayes, P.B. Berbon, and R.S. Mishra: *Metall. Mater. Trans. A*, 2004, vol. 35A, pp. 3855–61.
13. T.J. Van Daam and C.C. Bampton: US Patent, The Boeing Company, Chicago, IL, 2008.
14. O. Susegg, E. Hellum, A. Olsen, and M. Luton: *Micron Microsc. Acta*, 1992, vol. 23 (1/2), pp. 223–24.
15. Y. Li, W. Liu, V. Ortalan, W.F. Li, Z. Zhang, R. Vogt, N.D. Browning, E.J. Lavernia, and J.M. Schoenung: *Acta Mater.*, 2010, vol. 58 (5), pp. 1732–40.
16. F. Tang, C.P. Liao, B. Ahn, S.R. Nutt, and J.M. Schoenung: *Powder Metall.*, 2007, vol. 50 (4), pp. 307–12.
17. K.M. Youssef, R.O. Scattergood, K. Linga Murty, and C.C. Koch: *Appl. Phys. Lett.*, 2004, vol. 85 (6), p. 929.
18. K. Kumar, H. Van Swygenhoven, and S. Suresh: *Acta Mater.*, 2003, vol. 51 (19), pp. 5743–74.
19. E. Ma: *Scripta Mater.*, 2003, vol. 49 (7), pp. 663–68.
20. P.G. Sanders, J.A. Eastman, and J.R. Weertman: *Acta Mater.*, 1997, vol. 45 (10), pp. 4019–25.
21. Y. Wang, M. Chen, F. Zhou, and E. Ma: *Nature*, 2002, vol. 419 (6910), pp. 912–15.
22. G.J. Fan, H. Choo, P.K. Liaw, and E.J. Lavernia: *Acta Mater.*, 2006, vol. 54 (7), pp. 1759–66.
23. Z. Lee, V. Radmilovic, B. Ahn, E.J. Lavernia, and S.R. Nutt: *Metall. Mater. Trans. A*, 2009, vol. 41A (4), pp. 795–801.
24. L. Jiang, K. Ma, H. Yang, M. Li, E.J. Lavernia, and J.M. Schoenung: *JOM*, 2014, vol. 66 (6), pp. 898–908.
25. Y. Li, Y.H. Zhao, V. Ortalan, W. Liu, Z.H. Zhang, R.G. Vogt, N.D. Browning, E.J. Lavernia, and J.M. Schoenung: *Mater. Sci. Eng. A*, 2009, vol. 527 (1–2), pp. 305–16.
26. K.M. Reddy, P. Liu, A. Hirata, T. Fujita, and M.W. Chen: *Nat. Commun.*, 2013, vol. 4, p. 2483.
27. Z. Zhang, T. Topping, Y. Li, R. Vogt, Y. Zhou, C. Haines, J. Paras, D. Kapoor, J.M. Schoenung, and E.J. Lavernia: *Scripta Mater.*, 2011, vol. 65 (8), pp. 652–55.
28. Z. Zhang, S. Dallek, R. Vogt, Y. Li, T.D. Topping, Y. Zhou, J.M. Schoenung, and E.J. Lavernia: *Metall. Mater. Trans. A*, 2009, vol. 41A (2), pp. 532–41.
29. J.R. Davis: *Properties and Selection: Nonferrous Alloys and Special Purpose Materials*, 1990, ASM International, Metals Park, vol. 2.
30. P.W. Trimby: *Ultramicroscopy*, 2012, vol. 120, pp. 16–24.



31. P.W. Trimby, Y. Cao, Z. Chen, S. Han, K.J. Hemker, J. Lian, X. Liao, P. Rottmann, S. Samudrala, J. Sun, J.T. Wang, J. Wheeler, and J.M. Cairney: *Acta Mater.*, 2014, vol. 62, pp. 69–80.
32. Y. Zhang, T.D. Topping, E.J. Lavernia, and S.R. Nutt: *Metall. Mater. Trans. A*, 2013, vol. 45A (1), pp. 47–54.
33. Y.J. Li, W.Z. Zhang, and K. Marthinsen: *Acta Mater.*, 2012, vol. 60 (17), pp. 5963–74.
34. G. Lucadamo, N.Y.C. Yang, C.S. Marchi, and E.J. Lavernia: *Mater. Sci. Eng. A*, 2006, vol. 430 (1–2), pp. 230–41.
35. T.D. Topping, B. Ahn, Y. Li, S.R. Nutt, and E.J. Lavernia: *Metall. Mater. Trans. A*, 2011, vol. 43A (2), pp. 505–19.
36. J. Ye, B.Q. Han, Z. Lee, B. Ahn, S.R. Nutt, and J.M. Schoenung: *Scripta Mater.*, 2005, vol. 53 (5), pp. 481–86.
37. E.O. Hall: *Proc. Phys. Soc. Lond.*, 1951, vol. 64 (381), pp. 747–53.
38. N.J. Petch: *J. Iron Steel Inst.*, 1953, vol. 174 (1), pp. 25–28.
39. K. Peng, W. Chen, H. Zhang, and K.-W. Qian: *Mater. Sci. Eng. A*, 1997, vols. 234–236, pp. 138–41.
40. F. Tang and J.M. Schoenung: *Mater. Sci. Eng. A*, 2008, vol. 493 (1–2), pp. 101–03.
41. T.D. Topping and E.J. Lavernia: *13th International Conference on Aluminum Alloys*, John Wiley & Sons, Inc., Hoboken, NJ, 2012.
42. H. Yang, T.D. Topping, K. Wehage, L. Jiang, E.J. Lavernia, and J.M. Schoenung: *Mater. Sci. Eng. A*. DOI:[10.1016/j.msea.2014.07.079](https://doi.org/10.1016/j.msea.2014.07.079).
43. S.R. Nutt and J.M. Duva: *Scripta Metall.*, 1986, vol. 20 (7), p. 1055.
44. Y.H. Zhao, Y.Z. Guo, Q. Wei, T.D. Topping, A.M. Dangelewicz, Y.T. Zhu, T.G. Langdon, and E.J. Lavernia: *Mater. Sci. Eng. A*, 2009, vol. 525 (1–2), pp. 68–77.
45. B. Ahn, E.J. Lavernia, and S.R. Nutt: *J. Mater. Sci.*, 2008, vol. 43, p. 7403.
46. Z. Lee, D.B. Witkin, V. Radmilovic, E.J. Lavernia, and S.R. Nutt: *Mater. Sci. Eng. A*, 2005, vols. 410–411, pp. 462–67.
47. A.P. Newbery, S.R. Nutt, and E.J. Lavernia: *J. Miner. Met. Mater. Soc.*, 2006, vol. 58, pp. 56–61.
48. D.C. Hofmann, J.-Y. Suh, A. Wiest, G. Duan, M.-L. Lind, M.D. Demetriou, and W.L. Johnson: *Nature*, 2008, vol. 451 (7182), pp. 1085–89.
49. R.W. Hertzberg: *Deformation and Fracture Mechanics of Engineering Materials, Chapter 8*, Wiley, New York, 1996.
50. P.S. Pao, H.N. Jones, and C.R. Feng: *Mater. Res. Soc. Symp. Proc.*, 2004, vol. 791, p. Q1.8.1.